

# Tutorial: A practical guide to the alignment of defocused spatial light modulators for fast diffractive neural networks.

Guillaume Nœtinger,<sup>\*</sup> Tim Tuuva,<sup>\*</sup> and Romain Fleury<sup>†</sup>  
*Laboratory of Wave Engineering, Department of Electrical Engineering,  
 Ecole Polytechnique Fédérale de Lausanne (EPFL), 1015 Lausanne, Switzerland*  
 (Dated: November 13, 2025)

The conjugation of multiple spatial light modulators (SLMs) enables the construction of optical diffractive neural networks (DNNs). To accelerate training, limited by the low refresh rate of SLMs, spatial multiplexing of the input data across different spatial channels is possible maximizing the number of available spatial degrees of freedom (DoFs). Precise alignment is required in order to ensure that the same physical operation is performed across each channel. We present a semi-automatic procedure for this experimentally challenging alignment resulting in a pixel-level conjugation. It is scalable to any number of SLMs and may be useful in wavefront shaping setups where precise conjugation of SLMs is required, e.g. for the control of optical waves in phase and amplitude. The resulting setup functions as an optical DNN able to process hundreds of inputs simultaneously, thereby reducing training times and experimental noise through spatial averaging. We further present a characterization of the setup and an alignment method.

## I. INTRODUCTION

Advances in artificial intelligence (AI) have brought the field to the forefront of contemporary scientific research, with applications ranging from the generalization of large language models to the prediction of protein structures. To address more complex scientific or technical problems, neural networks are becoming increasingly complex [1]. In the context of a widespread AI deployment, concerns are being raised about its ecological impact [2] and the predicted future limitations of computing capacity due to the saturation of Moore’s law [3]. As a result, the previously overlooked domain of *optical computing* [4, 5] is experiencing a revival with a rapidly growing community in recent years [6].

An experiment based on the propagation of microwaves demonstrated that the propagation of a wave through a succession of carefully engineered layers can perform inference passively, similar to an artificial neural networks [7], as schematically depicted on Fig. 1.a. In this experiment, a microwave field is sent to a 3D-printed diffractive medium and, depending on the input pattern, is focused at a different position. This proves that waves can perform tasks currently reserved for numerical machine learning systems, such as *classification*, but in a passive way with no energy cost associated to the input processing. These results sparked a novel research axis in so-called *diffractive neural networks* (DNN) [8–10]. Using large wavelengths in the radio range allows to engineer precisely the propagation media relatively to the wavelength but results in cumbersome and slow experimental setups [11], with no available free-field source and no reconfigurability. Consequently, it becomes desir-

able to downscale the experiments to lightwaves, taking advantage of the favourable scaling of free-field optics [6]. The large number of reconfigurable spatial DoFs of SLMs or diffractive plates [12] as well as the wide bandwidth of optical waves [6] and the impressive *analog computing* abilities of full-field optics, such as the well-known 2D Fourier transform achieved at the speed of light by a simple lens [13], are particularly interesting features for DNN.

An optical equivalent of this seminal microwave experiment involves a succession of SLMs [9, 14] or the conjugation of successive SLMs with some *defocus* simply obtained by translating the SLM in the image plane by a distance  $\Delta z$  to account for the free-space propagation [15], thereby mimicking diffraction in a reconfigurable layered medium [16, 17] except for the filtering of the angular spectrum from the limited numerical aperture (NA) of the lenses. Although this approach attracts theoretical interest [18] it has not, to our knowledge, been realized experimentally. The closest realization of this type of architecture is found in a multi-plane light converter (MPLC) configuration [19] which uses multiple reflections on the same SLM with a reflective layer [20, 21] as shown in Fig. 1.b. This is achieved at the expense of many DoFs as the SLM must be partitioned into several zones. There is also a coarser control of the diffraction between two reflections, since the spacing between the SLM and the mirror must be large enough for sending the input but small enough to ensure that diffraction remains moderate and does not direct too much optical power outside the collecting optics. Finally, there is a low tolerance to minor misalignments [22].

The typical refresh rate for an SLM is 60Hz. For a batch of 60 000 images, sent one at a time, such as the standard  $28 \times 28$  pixels<sup>2</sup> MNIST image dataset used for classification and trained over 100 epochs, neglecting the optical-to-electronic conversion and processing time, this results in more than 27 hours of computation for each

<sup>\*</sup> These two authors contributed equally

<sup>†</sup> romain.fleury@epfl.ch

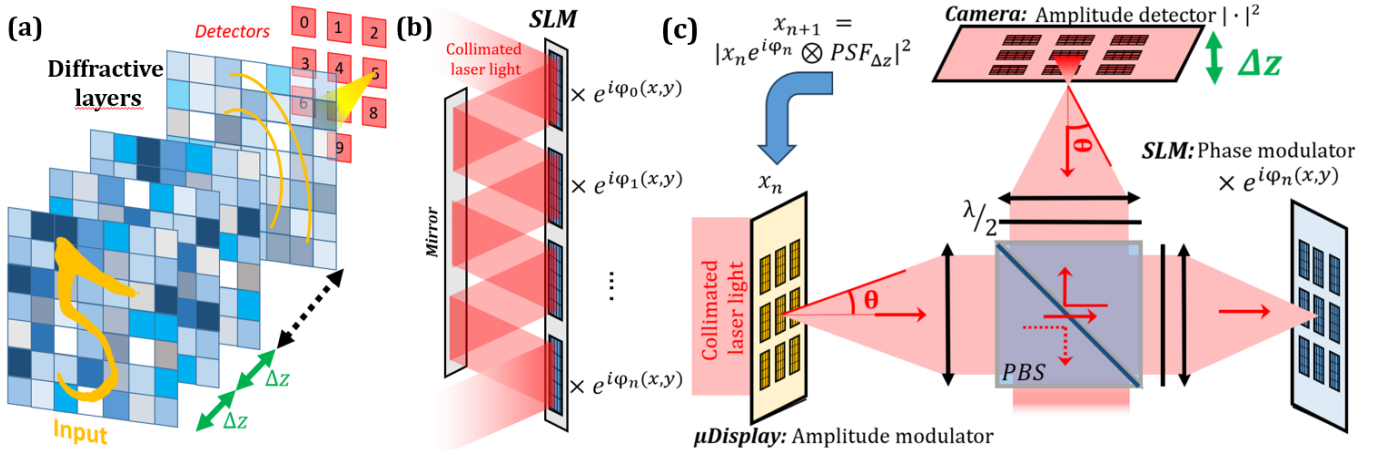


FIG. 1. **An optical diffractive neural network** (a) The wave associated to the image of a given digit is sent on the corresponding detector by properly tuning the propagation media, forming a *diffractive processor* [Ozcan] (b) A multi-plane light converter (MPLC) can perform an equivalent transformation for a light field but at the expense of a complicated alignment, low yield and the sacrifice of many degrees of freedom (DoFs). (c) The proposed setup consist in conjugated amplitude and phase modulators sent to a defocused camera at a distance  $\Delta z$  from the image plane, the resulting intensity is sent again onto the setup to be modulated again. Given the typical machine learning image size compared to the SLM resolution, multiple inputs can be displayed at the same time (here  $3 \times 3$  images,  $10 \times 10$  in our experiments) to speed up the acquisition.

layer i.e. propagation through the optical setup. Similar orders of magnitude for processing times have been reported in the literature in systems with less DOFs [23]. A possibility to enhance the speed of this optical DNN is to use spatial multiplexing, by displaying many different inputs simultaneously making the most out of the high number of spatial DoFs. If it is possible to display 100 inputs at a time, the training time decreases to 27 minutes per layer for 100 epochs. This can be achieved by dividing each modulator surface into different regions of interest (ROIs). However, it is necessary to ensure that each channel performs exactly the same physical operation. For this, two corresponding ROIs of successive modulators need to be perfectly and similarly aligned. Indeed, this transition to optical waves is not straightforward: as the wavelength decreases to the visible range, e.g. approximately 500 nm, so does the typical tolerance for the mechanical precision and the level of control of the propagation medium. For a full-field setup, this presents significant experimental challenges in terms of alignment, as is the case for MPLCs [24].

In this article, we present the equivalent of a DNN created by aligning an amplitude and phase modulator, which is sent to a defocused camera (see Fig. 1.c). The recorded data can then be sent through the setup again to mimic a multilayer neural network. The standard read-out non-linearity of the camera acts as a non-linearity added to each propagation through the setup, making this approach closer to a real digital neural network compared to a succession of diffractive plates.

The conjugation is performed using manual alignments followed by an automated procedure for precise fine-tuning, resulting in pixel-wise alignment. This procedure is robust to mild defocus and is therefore suit-

able for diffractive neural networks as a single reconfigurable diffractive layer, with additional non-linearity arising from the intensity sensitivity of the camera, as in a convolutional neural network (CNN) (see Fig. 1.c). It is scalable to an arbitrary number of conjugated or defocused SLMs by applying the same procedure to each modulator. As such, it can be used, for instance, to better align the different diffractive zone of a MPLC to reduce the mismatch with numerical simulation. Furthermore, a defocused conjugation of multiple spatial light modulators, by enabling the tailoring of optical wavefronts over large fields of view in both the real domain and angular spectrum, may benefit other optical applications [25, 26] such as the control of wave propagation in complex media [27], optical telecommunications [28], holography [29] or imaging setups [30, 31].

## II. THE ALIGNMENT PROTOCOL

### A. The setup

The setup is schematically shown in Fig. 1.a and depicted in more detail in Fig. 2. A red laser beam at 633 nm is expanded using a  $4f$ -system (lens  $L_0$ , not shown here, and  $L_1$ ). The resulting plane wave is directed to an amplitude modulator (Holoeye microdisplay HEO 2220 CFS with a  $4.5\mu\text{m}$  pixel pitch, hereafter referred to as the  $\mu\text{Display}$ ) conjugated with a phase-only modulator (Holoeye ERIS with an  $8\mu\text{m}$  pixel pitch, hereafter referred to as the SLM) using a  $4f$ -system. The resulting beam is then imaged onto a camera after polarization filtering in a conjugate plane. A diaphragm allows filtering of high spatial frequencies in the Fourier plane to

reduce the experimental noise. Another use of this diaphragm may be to obtain a tunable speckle grain size (see SI). We define the point-spread functions (PSF) from the  $\mu$ Display to the SLM as  $PSF_1$  and from the SLM to the camera as  $PSF_{\Delta z}$ . A grid of  $10 \times 10$  independent RoIs of size  $64 \times 64$  pixels each is used. This corresponds to more than  $4 \cdot 10^5$  DoF.

To accelerate the training of the DNN, these RoIs are used as parallel channels, each performing exactly the same operation. This enables batch training for each capture, increasing the training speed by a factor equal to the number of RoIs, in our case  $10^2$ . This requires that the same wavefield from the  $\mu$ Display is sent to a diffractive layer of the SLM with the same phase law for each channel. With the parameters chosen here, assuming a 60 Hz display and acquisition frequency - which is standard for the selected modulators and camera - and an output image of comparable size,  $64 \times 64$  pixels, each channel performs a multiplication with a Toeplitz matrix approximately of size  $64^2 \times 64^2$ . Overall, this is equivalent to  $64^4 \cdot 60 \cdot 100 \approx 10^{11}$  multiply-and-accumulate operations (MACs) per second, comparable to a standard graphics card from the 2000's [32].

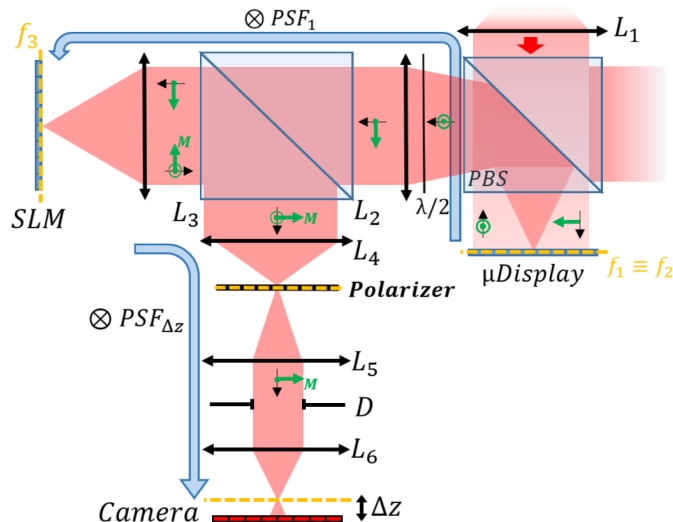


FIG. 2. **The setup.** An amplitude modulator (the  $\mu$ Display) is conjugated to a phase modulator (the SLM) using a  $4f$  system. The resulting field is sent to a defocused camera after filtering by a diaphragm  $D$ . The polarization is indicated by the green arrows. Only the horizontal polarization is modified by the SLM (green letter  $M$ ). The remaining vertical polarization is filtered with a polarizer. The field on the SLM is the convolution of the  $\mu$ Display's image and a point spread function (PSF)  $PSF_1$ , the propagation to the defocused camera corresponds to a convolution by  $PSF_{\Delta z}$ .

## B. The method

Our method relies on the diffraction of light by a sharp edge on the SLM. Between two zones of different voltage on the SLM, i.e. different refractive index, the sharp change in refractive indices diffracts some

light, which thus appears dark in a conjugate plane. Therefore, although the SLM is a phase modulator, any phase pattern results in a modification of the collected intensity in a conjugate plane. For instance, on Fig. 3.c targets are displayed on the SLM with the phase difference varying from 0 outside the target to  $2\pi$  at the center of each target, making the edges clearly visible. By using a camera positioned near a conjugate plane of the  $\mu$ Display and SLM, it is possible to align the SLM and the  $\mu$ Display manually. However, the precision of a manual alignment is limited. This edge can then be detected using standard detection algorithms, such as ellipse fitting provided by the *OpenCV* Python package [33] for fine-tuning the alignment. To improve detection efficiency, a set of concentric circles with alternating retardance of 0 or  $2\pi$  is displayed on the SLM instead of a single circle. The image of a dark disk is observed, it is easier to fit than a circle.

The corresponding code is available on GitHub [<https://github.com/TTimTT/SLM-alignment>] along with a video showing the calibration process for a  $N_{mux} = 8 \times 8$  grid. To ensure the two modulators are perfectly conjugated, one must proceed as follows:

1. **SLM positioning** Set the magnification of the  $4f$  system to exactly match the ratio of pixel pitches. As it is not possible to find two lenses with focal lengths in this exact ratio from standard catalogues, adjust the relative positions of the two lenses and objects to build a  $4f$  system with custom magnification. Position a camera at the conjugate plane of the  $\mu$ Display in place of the SLM (Fig. 3.a). Adjust the distances in the  $4f$  system  $L_2L_3$  iteratively so that the observed image on the camera matches the required magnification (Fig. 3.b). At the end of the process, measure the position of the camera's sensor relative to  $L_3$ .
2. **Manual alignment.** Roughly position the SLM at the previous location of the camera's sensor, close to conjugation with the  $\mu$ Display.
  - (a) Adjust the position of the SLM thanks to a six-axis translation and rotation stages (e.g. Thorlabs K6XS here) to align it with the  $\mu$ Display. For this purpose, display a uniform square pattern on the  $\mu$ Display and targets on the SLM whose edges are visible due to the sharp change in refractive index (see Fig. 3.c).
  - (b) Set the position of the SLM along the optical axis so that it is in the image plane of the  $\mu$ Display within the depth of field. Display alternate targets and squares of uniform intensity on the  $\mu$ Display and the opposite alternation on the SLM. Determine the position of the image planes of the SLM and  $\mu$ Display by translating the camera. Based on

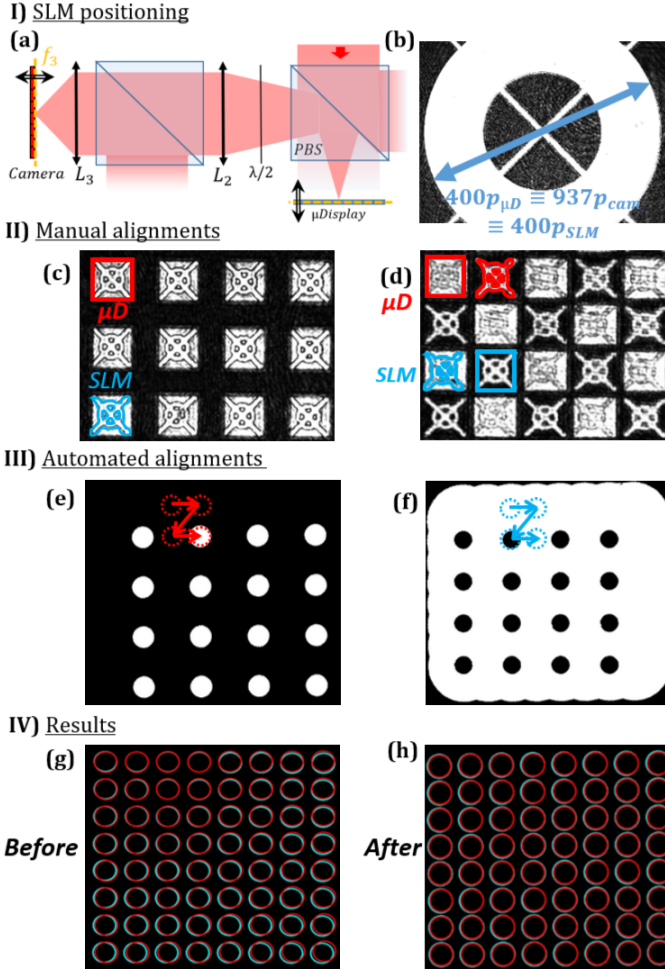


FIG. 3. **The alignment process.** (a) The SLM is replaced by a camera to locate the position of the  $\mu$ Display’s image plane and adjust the magnification of the  $4f$  system. (b) The magnification of the  $4f$  system is set by displaying a circle of known width on the  $\mu$ Display and measuring the resulting image width on the camera. **Manual alignments** (c) Lateral positioning: targets displayed on the SLM are manually aligned with square of uniform intensities on the  $\mu$ Display. (d) Axial positioning: when the SLM is conjugated to the  $\mu$ Display, clear images of resolution targets are observed on both modulators. **Automated alignments:** (e) Disks of uniform intensity are displayed on the  $\mu$ Display. To avoid any overlap if the camera is defocused and minimize the flux, only one disk out of four is displayed at a time so that each disk’s image never overlaps with their neighbors. Examples of the successive position of the disks for the four acquisitions are shown as yellow circles here. (f) Disks of alternating indices displayed on the SLM appears opaque on the camera due to wave diffusion by sharp edges and can be detected by standard ellipse fitting algorithm. Examples of the successive position of the disks for the four acquisitions are shown as blue circles here. **Results:** (g) Resulting calibrated surface: Each zone of the  $\mu$ Display (in red) and SLM could not be perfectly aligned manually due to limited precision in translation and rotation. (h) They match almost perfectly after using our algorithm.

their relative positions, translate the SLM forward or backward along the optical axis (see SI). When sharp images of the targets from both the SLM and  $\mu$ Display are obtained (see

Fig. 3.d), it indicates the two modulators are nearly conjugated with a precision being the depth of field of lens  $L3$ .

(c) Iterate between the two previous settings.

### 3. Automated alignments.

- (a) Display disks on the amplitude modulator while maintaining a flat phase on the SLM (Fig. 3.e). To prevent any overlap if the camera is defocused, only one disk out of four is displayed at a time, ensuring that each disk’s image never overlaps with its neighbors. Four separate acquisitions, each corresponding to a quarter of the disks, are then performed. On Fig. 3.e & 3f, the successive positions of four detected disks are shown using dotted lines, illustration the acquisition scheme used. A video is available at [<https://github.com/TTimTT/SLM-alignment>].
- (b) Record the centres of the disks on the camera by performing ellipse fitting.
- (c) Display a uniform intensity on the  $\mu$ Display and display concentric patterns on the SLM that appear as black circles on a white background. (Fig. 3.f)
- (d) Record the centres of the circles on the camera by performing ellipse fitting.
- (e) Apply shifts by comparing the positions of the disks associated with the  $\mu$ Display and the SLM.
- (f) Repeat steps (c-e) until the algorithm converges.

In the end, the RoIs of the  $\mu$ Display and SLM which were not matching (Figure 3.g) corresponds as shown on Figure 3.h and the center positions of each disk on the camera are recorded. To obtain the  $(x, y)$  coordinates where the RoIs are located, the average disk width is calculated and extended by a few pixels (4 here) in each direction to account for any mismatch in the calibration, noise and defocus, giving the number of output pixels  $N_{out} = N_{x,im} \cdot N_{y,im}$ . For each acquisition, when a shot is taken, it is cropped at each recorded position. Finally, all the cropped images from one single shot are assembled as a batch of images with size  $N_{mux} \cdot N_{x,im} \cdot N_{y,im}$ . This format makes it readily usable by *Pytorch* as it is designed for batch training.

## III. OPTICAL CHARACTERIZATION

To assess whether this alignment procedure functions correctly and to quantify its precision, the accuracy of the ellipse detection is evaluated by acquiring the output images corresponding to a single illuminated pixel for each RoI over a wide range of defocus (see SI). This

is equivalent to acquiring the modulus squared of the system's PSF which is also relevant for training a digital twin of this experiment *in silico*. The precision of this algorithm is 1 pixel in the presence of noise and for various values of defocus (see SI). Next, the relative positions of the RoIs on the SLM with respect to those on the  $\mu$ Display are examined by applying a random phase pattern on the SLM and maintaining a constant illumination on the  $\mu$ Display, and analyzing the relative positions of the observed speckle-like pattern using autocorrelation. Autocorrelation is a well-known experimental method for tracking movement or deformation, employed for instance in Digital Image Correlation or Particle Image Velocimetry. If a given RoI on the SLM is shifted relative to its corresponding RoI on the  $\mu$ Display compared to another set of  $\mu$ Display and SLM RoIs (i.e. *a channel*) then the output speckle patterns of these two channels will be shifted relative to the other meaning a different operation is performed on each RoI. Otherwise, if the alignment is correct, the speckle patterns will have the same position, ensuring that all channels perform exactly the same operation.

As an experiment, identical random phase masks are displayed on the SLM for each RoI, with constant illumination from the  $\mu$ Display. The intensity observed on the camera is shown on Fig. 4.a. The positions of the resulting output speckle patterns before and after the calibration process are compared by finding the maximum of the cross-correlation between each image and the central image at coordinate (6,6) on the  $10 \times 10$  grid. Before calibration, the further an image is from the center, the more shifted each speckle pattern is (Fig. 4.b). Images too far from the center are too different for the cross-correlation to yield meaningful results (the maximum correlation between different speckles yields only the relative position of the illumination, which is 1 pixel here, determined by the precision of the ellipse fitting algorithm detailed in the SI). After calibration and except for a few outliers, the images are shifted by less than 2 pixels, as shown in Fig. 4.b. This precision can be attributed to the precision of the ellipse fitting algorithm. After calibration, the speckle patterns are on average 0.8 pixels apart, compared to 2.5 pixels before calibration. As shown on the histogram 4.c, more than 90% of them are below 1.5 pixels, which is below the diffraction limit, resulting in similar speckle-like outputs. Consequently, after calibration, the sum of each speckle-like pattern does not average out as a spatially incoherent sum, as seen in 4.a., but instead forms a speckle-like pattern similar to that observed in each RoI. This means that each RoI is indeed usable as a parallel channel to process information optically..pn

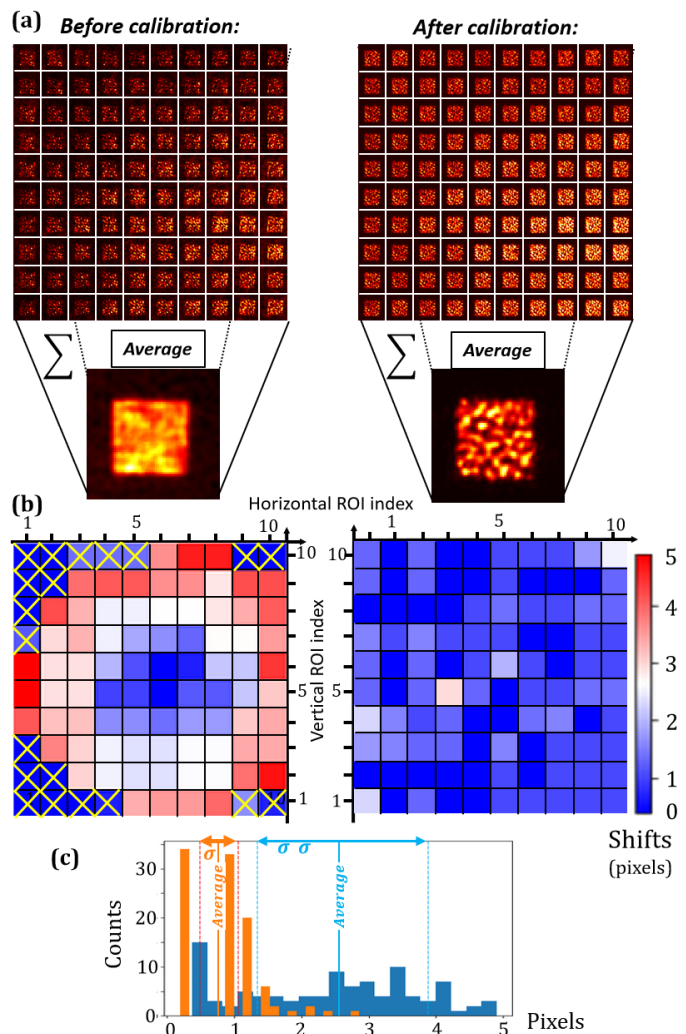


FIG. 4. **Comparison of the position of the speckle-like outputs before and after the automated alignment process.** (a) An example of raw speckle patterns and the average image. After calibration, the average image is a speckle-like pattern (right) whereas before calibration the sum averages to a square corresponding to the illuminated zone (left). (b) The number of shifts of each RoI compared to the central image measured with cross-correlation. The yellow cross indicates where the autocorrelation becomes irrelevant because the speckles patterns are too different. (c) A typical histogram of shifts: before the calibration, the images are shifted by up to 5 pixels (in blue). After calibration the images are shifted by less than 3 pixels, with the vast majority being shifted by 0 or 1 pixel (in orange).

## IV. ADVANTAGES FOR A DNN

### A. DNN structure and training

The DNN examined consists of three layers, corresponding to three propagations through the setup. To train this DNN, we attempted the following:

- Training a digital twin based on a physical model

by fitting the experimental PSF (see SI) and transferring the weight updates to the experiment [34].

- Training a digital twin using an experimental measurement of the transmission matrix in the Hadamard basis [35], with the loss incorporating the experimental output and transferring the weight updates to the experiment (see SI). Interestingly, thanks to our multiplexing method, it is possible to acquire the transmission matrices for  $N_{ROI} = 100$  RoIs of size  $N_{in} = 64 \times 64$  pixels<sup>2</sup> to the camera (an output image being approximately  $N_{out} = 80 \times 80$  pixels<sup>2</sup>) as quickly as for a single one. This measurement is completed in approximately 20 minutes and corresponds to  $N_{in} \cdot N_{out} \cdot N_{ROI} = 64^2 \cdot 80^2 \cdot 100 \approx 2.6 \cdot 10^9$  measurements.

As is already known from the state of the art [36], these methods, which are implicitly based on backpropagation are challenging to operate due to low noise tolerance and do not work in this case. We suspect that this system, which relies on full-field optics exhibits many parasitic reflections leading to input-dependent interference that makes training impossible, as the computed gradient differs too much from the experimental one. Finally, a supervised version of the forward-forward algorithm [37] is implemented. With this algorithm, the setup is used as an optical encoder [38]. Between each pass, fully-connected layers containing trainable weights are updated. For a simple classification problem such as MNIST, this algorithm requires two forward passes during training and ten forward passes during the inference. It is therefore slower than standard backpropagation. The detailed structure and parameters of the DNN are presented in the last section of SI.

### B. Effect on training and inference time

The evolution of the training time with the multiplexing is compared. Although an algorithm involving more propagation through the setup is used, the training time over 10 epochs is approximately 1 hour for 3 layers. Base on a 2 epochs experiment, a similar experiment displaying one image at a time takes around 4 days; the training time indeed decreases linearly with the number of images displayed. This makes it possible to train a DNN with optics in the visible range within a duration that is convenient for laboratory experiments. In addition, we posit that it might make the optical setup less sensitive to thermal or mechanical fluctuations since the training time has a characteristic time closer to the typical mechanical and thermal relaxation timescales. The score obtained is around 85% for MNIST digits classification dataset.

### C. Effect on the noise

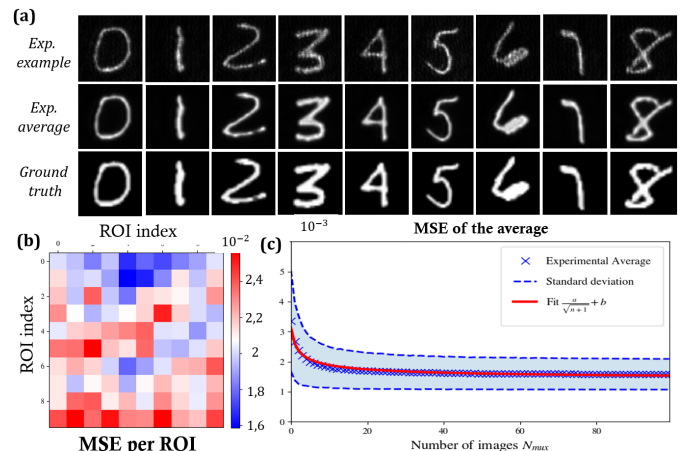


FIG. 5. **Effect of the multiplexing on the noise (a)** Experimental acquisition of MNIST digits on the setup in a conjugated configuration. **(b)** MSE to the mean image for each RoI. **(c)** Evolution of the noise with the number of images taken into account for averaging with standard deviation and fit.

In addition to accelerating the training process of a DNN by two orders of magnitude, this multiplexing scheme also has the beneficial effect of reducing the noise level through averaging. A simple experiment to demonstrate this behaviour is to display figures from the standard MNIST database on the  $\mu$ Display while maintaining a flat phase on the SLM with the camera being conjugated to both the SLM and  $\mu$ Display (see Fig. 5.a). This experiment is conducted over the entire MNIST digit dataset. First, the mean square error (MSE) for each channel, i.e. each RoI, is examined to verify whether some channels are more prone to noise. The MSE for each channel is computed and shown in Fig. 5.b, indicating that each has a similar noise level. The evolution of the MSE with the number of RoIs used for averaging is plotted in Fig. 5.c. It is fitted by a function of the form  $a + \frac{b}{\sqrt{n}}$  with  $a$  and  $b$  as adjustable parameters. Good agreement is observed, demonstrating that part of the noise is indeed random. The noise decreases below a threshold of  $2 \cdot 10^{-3}$ , reached for 30 approximately RoIs. This demonstrates another benefit of spatial multiplexing.

## V. CONCLUSION & PERSPECTIVES

In this article, we present a method to maximise the usable DoFs of an SLM to process large amounts of data in parallel leveraging the interesting scalability of full-field optics in terms of DoFs. Our setup consists of a conjugated amplitude and phase modulators receiving a plane wave, the output field is sent to a defocused camera. To achieve this, we have developed a procedure that

ensures each channel effectively performs the same physical operation. This is verified using constant illumination and random phase masks. The presented procedure can be readily applied to the conjugation of additional spatial modulators by successively translating the position of each RoI on each modulator relative to the previously calibrated modulator. This approach can accelerate the training of diffractive neural networks based on spatial light modulators and reduce experimental noise, although the noise level remains high enough to hinder training with the backpropagation algorithm. It may also be useful in other active research fields in optics where the conjugation of several spatial light modulators is of interest.

Training such a diffractive neural network is challenging especially if it relies on full-field optics and coherent light. It remains an open scientific question and is therefore a very active area of research [36]. This experiment mimics propagation in layered media with nonlinear effects and all the noise expected from such systems. It offers the scalability of full-field optics [6] in a

highly flexible configuration, with data blending determined by the defocus level and the diaphragm diameter, the number of DoFs set numerically, high training speed, and a tunable noise level enabled by the spatial multiplexing described here. Therefore, we believe this is an ideal platform for investigating this scientific question and for bridging the fields of optics and machine learning in a quantitative manner. Experimentally addressing the limitations of spatial light modulators [39] such as phase deformation from non-planarity [40], wavelength dependence [41], pixel crosstalk [42] but also parasitic reflections and multiple diffusion may provide a route to building efficient diffractive neural networks using wave propagation in structured media.

## ACKNOWLEDGMENTS

We thank Dr. Sébastien Popoff for his advises and addressing us to this journal.

- 
- [1] N. e. a. Maalej, Artificial intelligence index report 2024.”, Nature Reviews Physics <https://aiindex.stanford.edu/report/>. (2024).
- [2] P. Dhar, The carbon impact of artificial intelligence, Nature Machine Intelligence **2**, 423 (2020).
- [3] M. M. Waldrop, The chips are down for moore’s law, Nature **530**, 144 (2016).
- [4] R. Athale and D. Psaltis, Optical computing: Past and future, Opt. Photon. News **27**, 32 (2016).
- [5] J. Goodman, Optical computing — an overview, in *Topical Meeting on Optical Computing* (Optica Publishing Group, 1987) p. MA1.
- [6] P. L. McMahon, The physics of optical computing, Nature Reviews Physics **5**, 717 (2023).
- [7] X. Lin, Y. Rivenson, N. T. Yardimci, M. Veli, Y. Luo, M. Jarrahi, and A. Ozcan, All-optical machine learning using diffractive deep neural networks, Science **361**, 1004 (2018).
- [8] G. Wetzstein, A. Ozcan, S. Gigan, S. Fan, D. Englund, M. Soljačić, C. Denz, D. A. B. Miller, and D. Psaltis, Inference in artificial intelligence with deep optics and photonics, Nature (2020).
- [9] T. Zhou, X. Lin, J. Wu, Y. Chen, H. Xie, Y. Li, J. Fan, H. Wu, L. Fang, and Q. Dai, Large-scale neuromorphic optoelectronic computing with a reconfigurable diffractive processing unit, Nature Photonics **15**, 367 (2021).
- [10] J. Hu, D. Mengü, D. C. Tzarouchis, B. Edwards, N. Enggheta, and A. Ozcan, Diffractive optical computing in free space, Nature Communications **15**, 1525 (2024).
- [11] F. Zangeneh-Nejad, D. L. Sounas, A. Alù, and R. Fleury, Analogue computing with metamaterials, Nature Reviews Materials **6**, 207 (2021).
- [12] H. Wang and R. Piestun, Dynamic 2d implementation of 3d diffractive optics, Optica **5**, 1220 (2018).
- [13] J. W. Goodman, *Introduction to Fourier Optics*, 3rd ed. (Roberts & Company, 2005).
- [14] S. Chen, Y. Li, Y. Wang, H. Chen, and A. Ozcan, Optical generative models, Nature **644**, 903 (2025).
- [15] R. Chen, Y. Tang, J. Ma, and W. Gao, Scientific computing with diffractive optical neural networks, Advanced Intelligent Systems, Wiley 10.1002/aisy.202300536 (2023).
- [16] C. C. Wanjura and F. Marquardt, Fully nonlinear neuromorphic computing with linear wave scattering, Nature Physics **20**, 1434 (2024).
- [17] O. Kulce, D. Mengü, Y. Rivenson, and A. Ozcan, All-optical information-processing capacity of diffractive surfaces, Light: Science & Applications **10**, 25 (2021).
- [18] B. Savinson, D. J. Norris, S. Mishra, and S. Lanthaler, Universality of physical neural networks with multivariate nonlinearity, arXiv (2025), 2509.05420.
- [19] Y. Zhang and N. K. Fontaine, Multi-plane light conversion: A practical tutorial (2023), arXiv:2304.11323 [physics.optics].
- [20] Q. Jia, B. Shi, Y. Zhang, H. Li, X. Li, R. Feng, F. Sun, Y. Cao, J. Wang, C.-W. Qiu, M. Gu, and W. Ding, Partially coherent diffractive optical neural network, Optica **11**, 1742 (2024).
- [21] M. Yildirim, N. U. Dinc, I. Oguz, D. Psaltis, and C. Moser, Nonlinear processing with linear optics, Nature Photonics **18**, 1076 (2024).
- [22] J. C. A. Rocha, U. G. Bütaité, J. Carpenter, and D. B. Phillips, Self-configuring high-speed multi-plane light conversion (2025), arXiv:2501.14129 [physics.optics].
- [23] T. Onodera, M. M. Stein, B. A. Ash, M. M. Sohoni, M. Bosch, R. Yanagimoto, M. Jankowski, T. P. McKenna, T. Wang, G. Shvets, M. R. Shcherbakov, L. G. Wright, and P. L. McMahon, Scaling on-chip photonic neural processors using arbitrarily programmable wave propagation, preprint arXiv:2402.17750 (2024).
- [24] O. Lib, R. Shekel, and Y. Bromberg, Building and aligning a 10-plane light converter, Journal of Physics: Photonics **7**, 033001 (2025).

- [25] S. Gigan, O. Katz, H. B. de Aguiar, E. R. Andresen, A. Aubry, J. Bertolotti, E. Bossy, D. Bouchet, J. Brake, S. Brasselet, Y. Bromberg, H. Cao, T. Chaigne, Z. Cheng, W. Choi, T. Čížmár, M. Cui, V. R. Curtis, H. Defienne, M. Hofer, R. Horisaki, R. Horstmeyer, N. Ji, A. K. LaViolette, J. Mertz, C. Moser, A. P. Mosk, N. C. Pégard, R. Piestun, S. Popoff, D. B. Phillips, D. Psaltis, B. Rahmani, H. Rigneault, S. Rotter, L. Tian, I. M. Vellekoop, L. Waller, L. Wang, T. Weber, S. Xiao, C. Xu, A. Yamilov, C. Yang, and H. Yilmaz, Roadmap on wavefront shaping and deep imaging in complex media, *Journal of Physics: Photonics* **4**, 042501 (2022).
- [26] K. Y. Bliokh, E. Karimi, M. J. Padgett, M. A. Alonso, M. R. Dennis, A. Dudley, A. Forbes, S. Zahedpour, S. W. Hancock, H. M. Milchberg, S. Rotter, F. Nori, K. Özdemir, N. Bender, H. Cao, P. B. Corkum, C. Hernández-García, H. Ren, Y. Kivshar, M. G. Silveirinha, N. Engheta, A. Rauschenbeutel, P. Schneeweiss, J. Volz, D. Leykam, D. A. Smirnova, K. Rong, B. Wang, E. Hasman, M. F. Picardi, A. V. Zayats, F. J. Rodríguez-Fortuño, C. Yang, J. Ren, A. B. Khanikaev, A. Alù, E. Brasselet, M. Shats, J. Verbeeck, P. Schattschneider, D. Sarenac, D. G. Cory, D. A. Pushin, M. Birk, A. Gorchach, I. Kaminer, F. Cardano, L. Marrucci, M. Krenn, and F. Marquardt, Roadmap on structured waves, *Journal of Optics* **25**, 103001 (2023).
- [27] S. Rothe, K. Wisal, C.-W. Chen, M. Ercan, A. Jesacher, A. D. Stone, and H. Cao, Output beam shaping of a multimode fiber amplifier, arXiv (2024), 2410.23361.
- [28] N. U. Dinc, M. Yildirim, I. Oguz, C. Moser, and D. Psaltis, Multicasting optical reconfigurable switch (2024), arXiv:2401.14173 [physics.optics].
- [29] Roadmap on holography, *Journal of Optics* **22**, 123002 (2020).
- [30] C. Maurer, A. Jesacher, S. Bernet, and M. Ritsch-Marte, What spatial light modulators can do for optical microscopy, *Laser & Photonics Reviews* **5**, 81 (2011).
- [31] G. Neetinger, F. Lemoult, and S. M. Popoff, Dynamic structured illumination for confocal microscopy, *Opt. Lett.* **49**, 1177 (2024).
- [32] .
- [33] G. Bradski, The OpenCV Library, Dr. Dobb's Journal of Software Tools (2000)].
- [34] L. G. Wright, T. Onodera, M. M. Stein, T. Wang, D. T. Schachter, Z. Hu, and P. L. McMahon, Deep physical neural networks trained with backpropagation, *Nature* **601**, 549 (2022).
- [35] S. M. Popoff, G. Lerosey, R. Carminati, M. Fink, A. C. Boccara, and S. Gigan, Measuring the transmission matrix in optics: An approach to the study and control of light propagation in disordered media, *Phys. Rev. Lett.* **104**, 100601 (2010).
- [36] A. Momeni, B. Rahmani, B. Scellier, L. G. Wright, P. L. McMahon, C. C. Wanjura, Y. Li, A. Skalli, N. G. Berloff, T. Onodera, I. Oguz, F. Morichetti, P. del Hougne, M. Le Gallo, A. Sebastian, A. Mirhoseini, C. Zhang, D. Marković, D. Brunner, C. Moser, S. Gigan, F. Marquardt, A. Ozcan, J. Grollier, A. J. Liu, D. Psaltis, A. Alù, and R. Fleury, Training of physical neural networks, *Nature* **645**, 53 (2025).
- [37] A. Momeni, B. Rahmani, M. Malléjac, P. del Hougne, and R. Fleury, Backpropagation-free training of deep physical neural networks, *Science* **382**, 1297 (2023).
- [38] F. Xia, K. Kim, Y. Eliezer, L. Shaughnessy, S. Gigan, and H. Cao, Deep learning with passive optical nonlinear mapping, ArXiv (2023).
- [39] A. Jullien, Spatial light modulators, *Photoniques* (2020).
- [40] D. Marco, A. Vargas, M. del Mar Sánchez-López, and I. Moreno, Measuring the spatial deformation of a liquid-crystal on silicon display with a self-interference effect, *Opt. Lett.* **45**, 4480 (2020).
- [41] G. Bold, T. Barnes, J. Gourlay, R. Sharples, and T. Haskell, Practical issues for the use of liquid crystal spatial light modulators in adaptive optics, *Optics Communications* **148**, 323 (1998).
- [42] S. Moser, M. Ritsch-Marte, and G. Thalhammer, Model-based compensation of pixel crosstalk in liquid crystal spatial light modulators, *Opt. Express* **27**, 25046 (2019).
- [43] J. Mertz, *Introduction to Optical Microscopy*, 2nd ed. (Cambridge University Press, 2019).
- [44] S. Popoff, Setting up a DMD/SLM: Aberration effects, www.wavefrontshaping.net (2016).
- [45] S. Popoff, G. Lerosey, A. C. Boccara, and S. Gigan, Image transmission through an opaque material, *Nature Communications* **1**, 81 (2010).
- [46] J. S. Heung-Chang Lee, Symba: Symmetric backpropagation-free contrastive learning with forward-forward algorithm for optimizing convergence, arXiv:2303.08418v1 (2023).
- [47] T. Akiba, S. Sano, T. Yanase, T. Ohta, and M. Koyama, Optuna: A next-generation hyperparameter optimization framework, (2019).

## SUPPLEMENTARY INFORMATIONS

### A. Axial positioning of the SLM

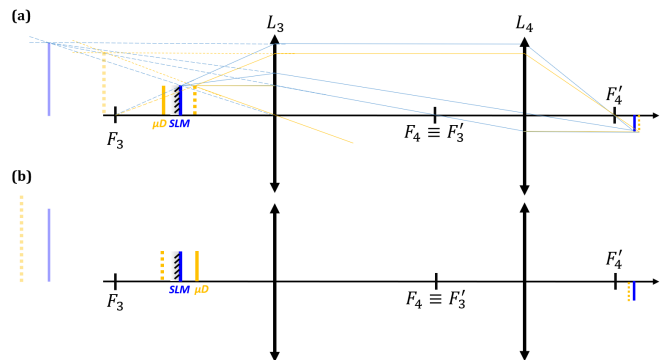


FIG. 6. **Optical scheme for the  $4f$  system conjugating the two modulators.** The  $\mu$ Display image from  $L_1 - L_2$  is indicated with a solid orange line at the left of the optical system, the SLM as a solid blue line with a mirror, the secondary image through the mirror and lens  $L_3$  are represented with dotted lines. **(a)** If the  $\mu$ Display image from  $4f$  system  $L_1 - L_2$  is located farther from the lense than the SLM image, it means that the  $\mu$ Display image needs to be translated toward lense  $L_3$ . **(b)** If the  $\mu$ Display image from  $4f$  system  $L_1 - L_2$  is located closer from the lense than the SLM image, it means that the  $\mu$ Display image (left, solid orange) needs to be translated away from lense  $L_3$ .

This step is not strictly necessary during the calibration procedure to function as it is robust to defocus, as shown previously. However, for the future of this experiment, in order to use machine learning and phase reconstruction algorithms it is useful to have a good initial guess of the field in this plane. Therefore, we aim to use the *simplest* possible configuration, in which the two modulators are approximately conjugated with a pixel-to-pixel matching.

Depending on the relative position of the images of the SLM and  $\mu$ Display after lens  $L_4$ , the relative position of the SLM and the  $\mu$ Display can be deduced, as shown in Fig. 6. The reflection from the reflective layer of the SLM must be taken into account. The SLM is translated according to the observed relative position of the images along the optical axis. At each step, the camera must also be translated again to locate the relative position of the two images. This iterative procedure converges to a state in which the images from the  $\mu$ Display and the edges of the images displayed on the SLM appear sharp.

### B. Ellipse detection efficiency & PSF acquisition

Squares of increasing width are displayed on the  $\mu$ Display for various values of defocus. The SLM phase-mask remains flat throughout the whole process. Similar PSF images are obtained on each RoI (see Fig. 7.a) confirming the correct alignment. For a single illuminated pixel, the PSF signal is above the noise but of comparable amplitude; for two pixels it is well resolved. From interference with an unmodulated background, the field is obtained as shown in the cross-section view (Fig. 7.b), this is highlighted by the fact that signal decrease below the background value similarly to an homodyne interferometric scheme [40]. For the conjugated case, the well-known Airy spot [43] is observed. For one and two pixels wide inputs, the two profiles are almost identical based on the positions of the zeros, as can be seen in the cross-section plot in Fig. 7.b (only the levels of the first secondary lobes differ slightly). However for a three pixel wide input, the profile begins to enlarge. This indicates that three pixels is approximately the diffraction limit of this setup from the  $\mu$ Display plane and that it is possible to use  $2 \times 2$  macropixels while remaining diffraction limited in order to achieve a higher signal. Negligible aberrations are visible, they are slightly more important in the RoIs far from the central zone of the camera where the paraxial approximation is less valid. For each value of defocus and input width, all images are summed to obtain average PSFs, as shown on Fig. 7.c. As the noises differs for each image, it cancels out when averaging and the signal-to-noise ratio (SNR) increases roughly by a factor of 10 when computing the average PSF. For each value of defocus, starting from a perfectly conjugated configuration to a large defocus, where the PSF main lobe is approximately 30 pixels wide, the PSF is experimentally measured. The position of the PSF obtained for each

RoI relatively to the average PSF is then examined by autocorrelation for each value of defocus. On Fig. 7.d. is represented the measured shift for each RoI to the average PSF in pixels. The maximum shift is 1 pixel in each direction leading to a maximum shift of  $\sqrt{2}$  pixels. In any case this is lower than the diffraction limit. We assume, it is the limit precision of the autocorrelation calculation in the presence of noise as shown in the next section. The number of shifted images augments with the defocus but stays around 1 pixel.

The theoretical PSF can be computed by propagating the wave from the image plane, where the field is the Airy spot, to the camera plane over a distance  $\Delta z$  using the Huygens-Fresnel principle. The predicted PSF match the experimental results (see below)

### C. Analytical formulation of the PSF and PSF fitting

The field from the image plane of the  $\mu$ Display is an Airy spot (whose dimensions are given by the limiting NA, here from lense  $L_3$  with the largest focal length). Applying the Huygens-Fresnel principle, it is integrated to obtain the field at the observation plane at a distance  $\Delta z$  [Born&Wolf] :

$$PSF_{\Delta z}(\vec{r}) \propto \Delta z \cdot \iint PSF_0(\vec{r}_0) \cdot e^{j\frac{2\pi}{\lambda}l(\vec{r}_0)} \frac{dr_0}{l(\vec{r}_0)^2} \quad (1)$$

with  $l$  being the distance between the observation point and integration point:  $\vec{l} = \vec{r} + \Delta z \vec{z} - \vec{r}_0$  hence  $l = \sqrt{((x-x_0)^2 + (y-y_0)^2 + \Delta z^2)}$  and:

$$PSF_0(\vec{r}_0) \propto \frac{J_1(\frac{2\pi}{NA\lambda}r_0)}{r_0} \quad (2)$$

from the integration of the field originating from a lense available in classical textbooks of imaging optics [JMertz]. Thus Equation 1 writes:

$$PSF_{\Delta z}(\vec{r}) \propto \Delta z \cdot \iint \frac{J_1(\frac{2\pi}{NA\lambda}r_0)e^{j\frac{2\pi}{\lambda}\sqrt{((x-x_0)^2+(y-y_0)^2+\Delta z^2)}}}{r_0 \cdot ((x-x_0)^2 + (y-y_0)^2 + \Delta z^2)} dx_0 dy_0 \quad (3)$$

On Fig. 8 are shown the experimental average PSF (top) from the measurement on each RoI (e.g. Fig. 7.a.) and the theoretical PSF obtained from Equation 3 (bottom). A very good qualitative agreement is obtained between the two.

### D. High frequency filtering and tunability of the speckle grain thanks to the diaphragm

Spatial light modulators are not perfect components. They exhibit spatial non-uniformities from fabrication,

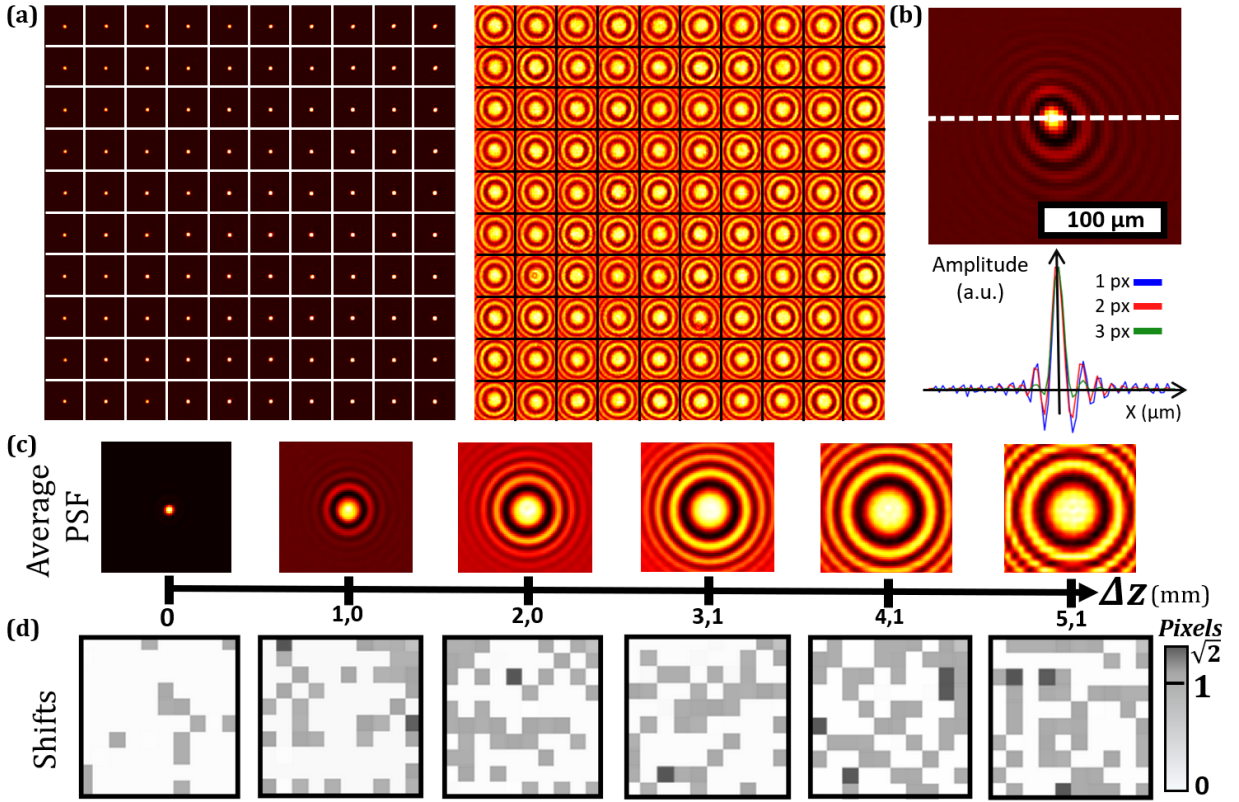


FIG. 7. **PSF acquisition and alignment.** (a) PSF acquisition on each ROI for a conjugated (left) and defocused configuration (right). (b) The average PSF obtained by summing all the images on each ROI for a slight defocus. (c) The experimental PSFs averaged over all ROIs for a varying defocus. (d) Shifts for each ROI in pixels measured by autocorrelation.

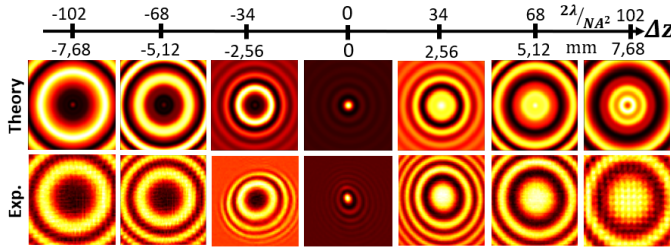


FIG. 8. **PSF fitting.** the experimental PSF (top) compared to the semi-analytical predictions (bottom) for positive and negative defocus expressed in mm and in terms of the depth of field ( $2\lambda/NA^2$ ).

a filling factor below 100% due to the necessary separation of liquid crystal pixels, and the voltage difference for each pixels is not perfectly confined in space to its area because of electromagnetic edge effects, leading to distorted wavefronts [44]. The optical index difference between neighboring liquid-crystal cells introduces edges capable of diffracting light as a grating. This mainly contributes to high spatial frequencies content of the collected images and *cross-talk* between ROIs as those index differences are sharp [31, 39]. This deviation from an ideal phase mask can be roughly modelled as a constant phase mask in the low spatial frequency range and

a variable, *i.e.* phase mask input dependent, high frequency noise. To mitigate the effect of the low frequency mask, the ROIs are sized smaller than the characteristic length of the constant phase mask characteristic length. To filter these high frequencies and suppress cross-talk, a diaphragm  $D$  is added in the Fourier plane of the modulators. We study the effects of this diaphragm diameter on the width of the PSF and the reduction of the MSE using constant illumination on the  $\mu$ Display and random phase masks on the SLM. The results are summarised up in Fig. 9.a. Closing the diaphragm filters out high frequencies and spurious signals thus lowering the MSE without degrading the PSF until a certain threshold value is reached, at which point the PSF begins to enlarge (Fig. 9.b). When this threshold is reached, it indicates that the NA of lens  $L_6$  becomes the limiting NA, whereas previously it was lens  $L_3$ . Whether this enlargement is desirable remains an open question. On one hand, it results in a loss of high spatial frequency content from the input and this loss of information [13] might be detrimental to the classification. On the other hand, the convolution with a larger PSF - or, in machine-learning terminology, a larger kernel- blends the data more effectively leading to a coarser speckle grain (Fig. 9.c).

As a compromise, the diameter is set at 3.8mm, just before this threshold.

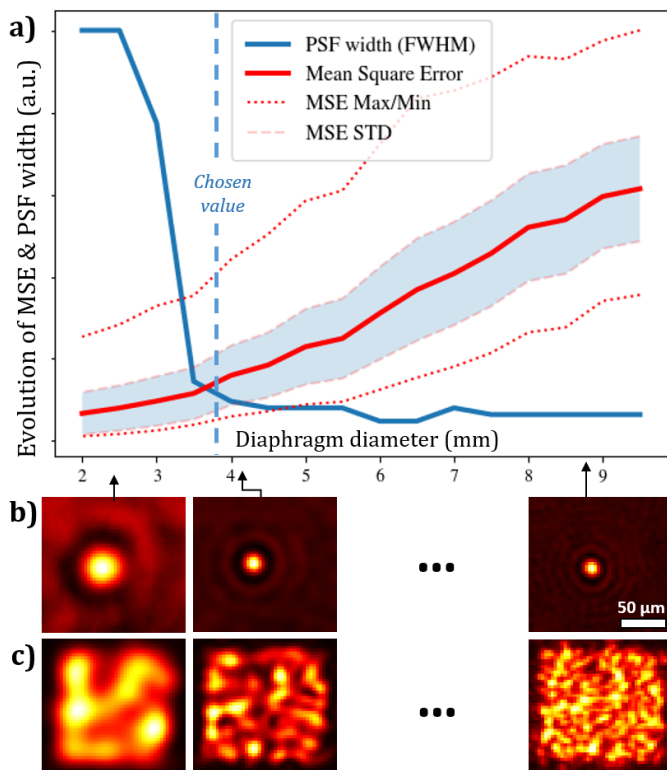


FIG. 9. **Effect of the diaphragm diameter:** Spatial variability of uniform inputs conjugated with random phase masks. (a) Spatial mean square error (MSE) and width of the point-spread function (PSF) as a function of the diaphragm filter  $F_2$  diameter. (b) Experimental PSF acquisitions obtained by summing the PSF on all spatial channels. (c) Example of images with constant illumination on a square zone and random phase masks. A reduction of the diaphragm diameter increases the size of the speckle grain.

### E. Transmission matrix measurements

The transmission matrix from the SLM to the camera is measured over each RoI using the algorithm described in [35], with the reflection on the glass cover of the SLM serving as a reference beam. The measurement of the PSF, shown in Fig. 7.b, indicates that this reflection is sufficiently strong to access the field by homodyne interferometry. As previously observed, the signal from  $2 \times 2$  pixels is similar to that from single pixels, but with a higher SNR in the PSF measurements. Therefore, we use the Hadamard basis on  $64 \times 64$  pixels RoIs with 2 pixels binning, meaning the basis contains  $32 \times 32 = 1024$  elements. There are  $10 \times 10$  RoIs so 100 transmission matrices are obtained. These matrices are similar one to another and can be condensed into an average matrix. Using a change-of-basis matrix, the matrix is converted to the pixel basis as shown in Fig. 10.a. In the pixel basis, a matrix with a dominant diagonal is obtained, this is expected for a defocused optical system. For no defocus and moderate defocus, the lines

of the matrix indeed corresponds to circular functions such as Airy spots, with or without defocus (Fig. 10.b). To verify that the obtained matrix  $M$  has physical significance, successful refocusing on a given pattern is achieved across all RoIs, as shown on Fig. 10.c, d & e. To achieve this, the matrix is filtered: only 10% of the highest eigenvalues returned by the SVD algorithm are kept and a pseudo-inverse  $iM$  is obtained by Tikhonov regularization  $iM = (M^* \cdot M + SNR)^{-1} \cdot M^*$ . The phase mask corresponding to a desired output is obtained by multiplying the output with  $iM$ . The refocusing on *simple* sparse patterns such as two dots (Fig. 10.c & d) is convincing, however when the patterns are more elaborate, such as a cross or a circle, the resulting output intensity exhibits significant deformations and artefacts (Fig. 10.d). This is explained by the fact that the flux equivalent to each pixel is too low to enable efficient focusing on complex patterns; as a result, the signal drops and the noise increases inversely [45]. This can be achieved using an average transmission matrix over all RoIs or for each RoI independently. In the latter case, the refocusing quality is significantly improved as can be seen in the average outputs depicted in Fig. 10.e, but the SVD, filtering, and inversion time increases from less than a minute to more than an hour, approximately scaling with the number of RoIs.

However, for random phasemasks displayed on the SLM, it is impossible to predict the output of the setup thanks to the transmission matrix. On Fig. 11 experimental outputs for a random phasemask on the SLM are depicted along the predicted output using the measured transmission matrix. There is a strong discrepancy between the two. Any filtering using the SVD operator has no influence on this result.

Our guess is that this phenomenon, already known from the literature [35, 45], hinders the possibility to compute a relevant phasemask using direct backpropagation, either using a convolutive model (with an analytical formula using a fitted version of the measured PSF at the previous section) or a model using the experimental matrix.

### F. Detailed neural network structure

After trying training with backpropagation, we implemented a Forward-Forward algorithm [37] where the optical setup is used as an optical encoder with fully connected layers in between two propagation on the optical setup. The full pipeline is represented on Fig. 12.

*a. Data labeling.* The data has to be labeled for the Forward-Forward algorithm to recognize correctly *vs.* incorrectly labeled data. To increase the inference score, we increase the energy associated to the label relatively to the energy associated to the data in terms of optical flux using *intrinsic class patterns* [46]. It consists, for

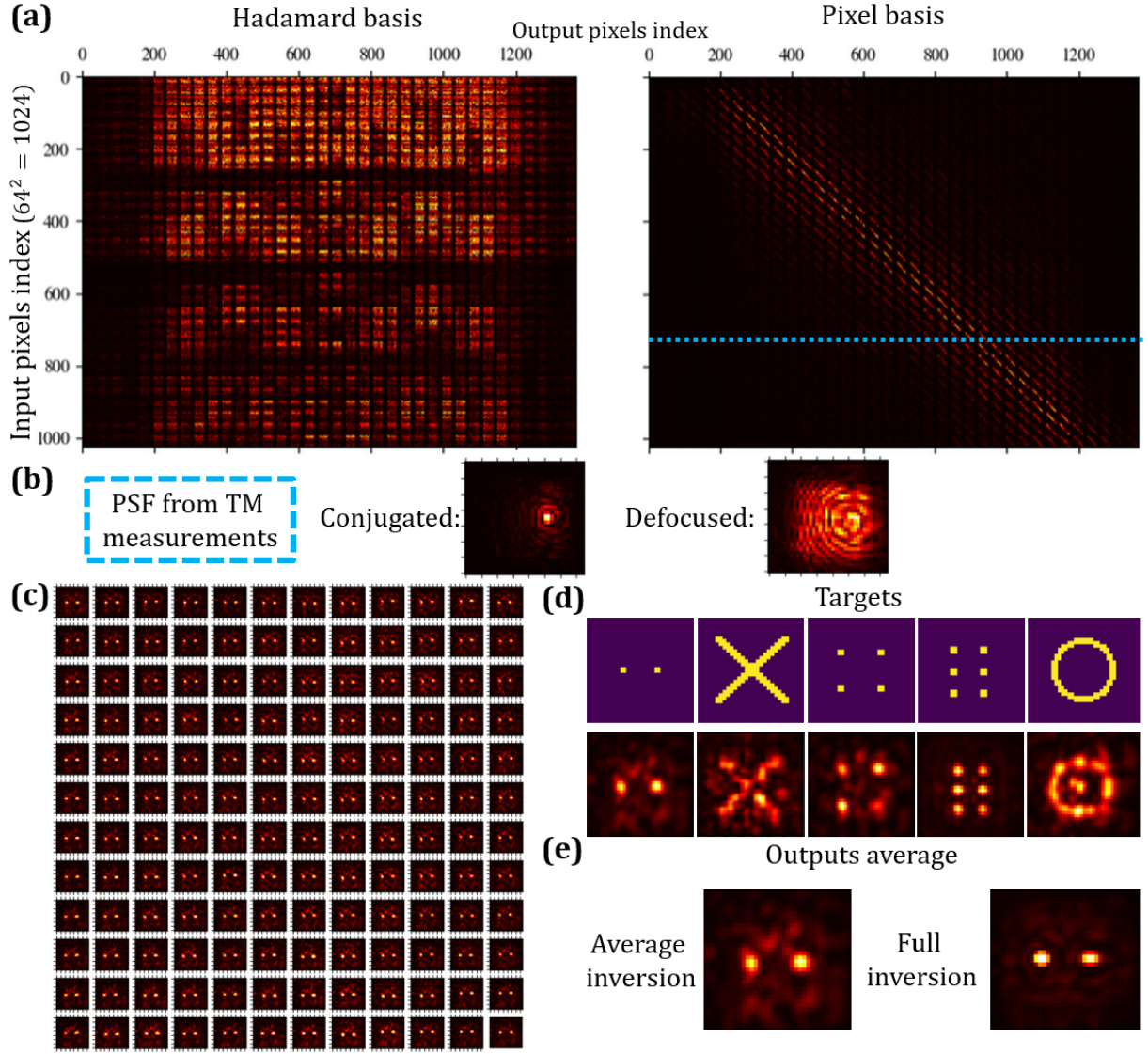


FIG. 10. **Transmission matrix measurements.** (a) The raw modulus of the transmission matrix in the Hadamard basis (left) and pixel basis (right). (b) One line of the TM represented as an image for conjugated (left) and defocused (right) configuration. (c) The refocusing on two points over all the RoI using the inverted transmission matrix averaged over all RoIs ( $\pm$  = spatial average). (d) The output average over all RoIs of the refocusing on different patterns (e) Comparison of the average output obtained for a two point targets with inversion of the average matrix (right) or the inversion of all the transmission matrix obtained for each RoI (right).

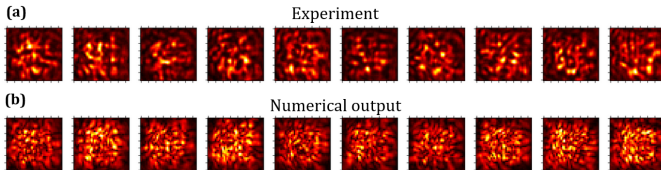


FIG. 11. **Random mask output** (a) Experimental. (b) Theoretical, from the measured transmission matrix output.

each label, in including the image in a random binary pattern instead of a one-hot vector. Therefore, the label information hidden in the data corresponds to the flux of

many pixels instead of a single one.

*b. Phase masks.* In this experiment, we use only static phase masks  $\phi^{(l)}$  identical for all subimages on the SLM. An interesting question would be to determine experimentally the best mask to differentiate the positive from the negative data but it is beyond the scope of this paper.

*c. Numerical layers.* The size of the transmission matrix in the numerical fully-connected (nFC) layers depends on the size of the subimages acquired  $N_{pix,in}$  and the size of the output data to be sent again in the setups  $N_{pix,out}$ . These two *hyperparameters* can be optimized for each applications thanks to the flexibility of our setup.

They could be used to perform data *augmentation* or *reduction* physically. Although the objective of this paper is not to study this option in detail, we provide an example of such an optimization in the results section below. For the chosen value of the diaphragm  $F_2$  diameter, the speckle grain size can be adjusted from 3 to 10 pixels using the diaphragm diameter. With the chosen value the speckle grain size is approximately 5. To reduce the size of the nFC matrix, an average 2D pooling is added with a reduction factor  $n_{pool}$  of 2 smaller than the speckle grain size ensuring that there is no loss of information. Conversely, for the next propagation step, the output is expanded using the opposite operation of *expanding* where one pixel is converted into  $n_{exp} \cdot n_{exp}$  pixels. Experimen-

tally, this makes the flux associated to one output of the nFC more important compared to the noise level. In addition, from the PSF measurements, we know that the setup is still diffraction limited for  $2 \times 2$  pixels inputs and that  $3 \times 3$  is an acceptable limit (see SI).  $n_{expand}$  is therefore set to 2.

*d. Hyperparameters optimization.* For different values of defocus, different values of hyperparameters may provide the best inference score. Hence, to provide an accurate comparison of the physical parameters influence, numerical hyperparameters giving the best inference score such as the choice of loss and activation function and learning rates must be chosen for each physical configurations. To automate this hyperparameter optimization, the *Optuna* package [47] is used.

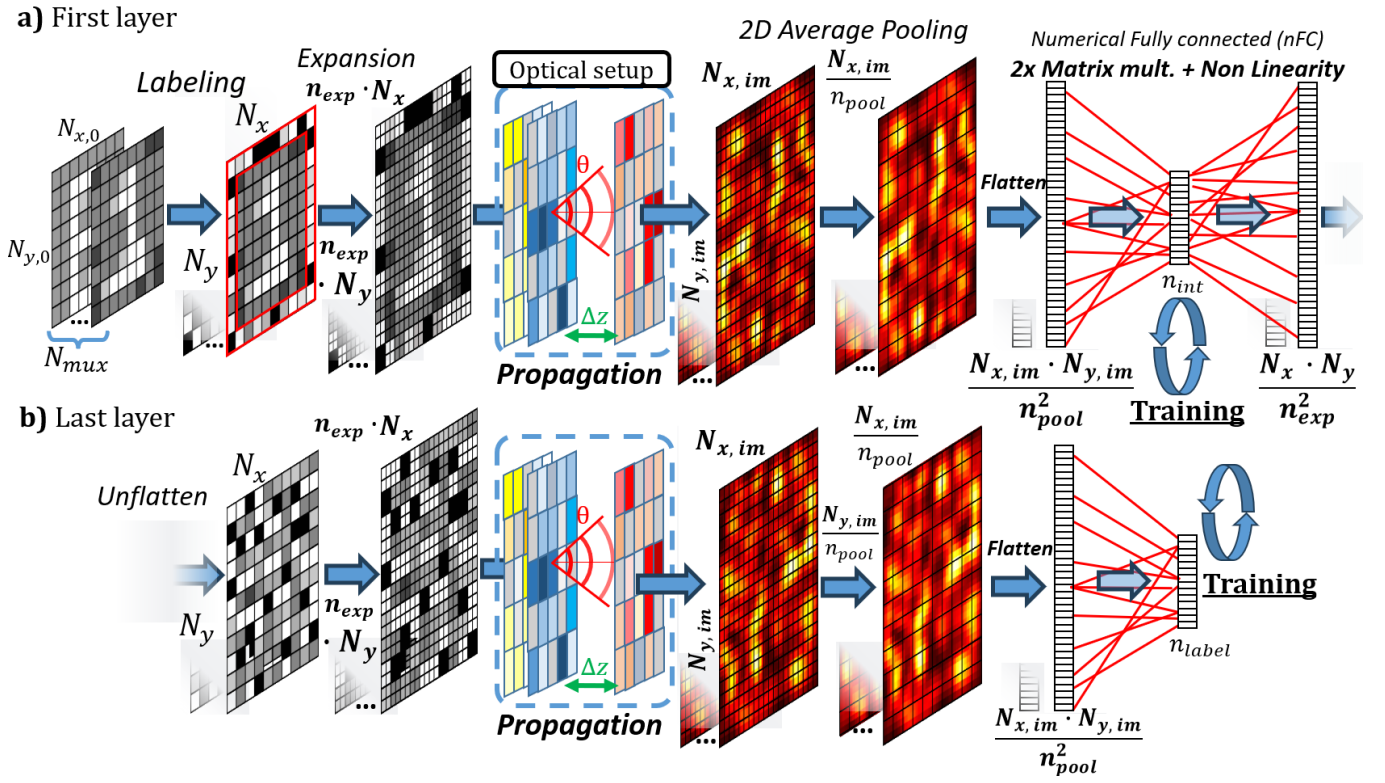


FIG. 12. **Full neural networks** depicted as a data pipeline for a depth  $n_l = 2$ . A batch of  $N_{mux}$  images of size  $N_{x,0} \times N_{y,0}$  is labeled and goes through the optical setup using the multiplexing procedure described in the main text. The resulting images are average pooled by a factor  $n_{pool}$  to match the speckle grain size and sent to numerical fully connected layers before being sent again to the setup for additional optical propagation steps. At each step, the data is expanded by a factor  $n_{exp}$  so that the information from one pixel is sent to more pixel to increase the flux and decrease the size of the intermediate numerical fully connected. The last layer maps the optical output to the number of expected categories  $n_{label}$